

A combined ocean and oil model for model-based adaptive monitoring*

Zak Hodgson^{a,*}, David Browne^b, Iñaki Esnaola^a, Bryn Jones^a

^aDepartment of Automatic Control and Systems Engineering, University of Sheffield, Sheffield, South Yorkshire, S1 3JD, United Kingdom

^bAndrew Moore & Associates, 2703 Universal Trade Centre, 3 Arbuthnot Road, Central, Hong Kong (SAR), China

Abstract

This paper presents a combined ocean and oil model for adaptive placement of sensors in the immediate aftermath of oil spills. A key feature of this model is the ability to correct its predictions of spill location using continual measurement feedback from a low number of deployed sensors. This allows for a model of relatively low complexity compared to existing models, which in turn enables fast predictions. The focus of this paper is upon the modelling aspects and in-particular the trade-off between complexity and numerical efficiency. The presented model contains relevant ocean, wind and wave dynamics for short-term spill predictions. The model is used to simulate the 2019 Grande America spill, with results compared to satellite imagery. The predictions show good agreement, even after several days from the initial incident. As a precursor to future work, results are also presented that demonstrate how sensor feedback mitigates the effects of model inaccuracy.

Keywords: Adaptive monitoring, Oil modelling, Contaminant monitoring

1. Introduction

The clean-up operations and legal claims that surround the annual average of 3500 (EMSA, 2018) maritime incidents and their lost cargo suffer from a lack of information, particularly in a remote location or in the immediate aftermath when current surveillance resources are unsuitable, unreliable or unavailable. While following a downward trend, around 6000 tonnes of oil are currently lost per year, with a 24 year peak of 116,000 tonnes in 2018 (ITOPF, 2019). Clean-up operations, accident monitoring and rescue attempts are often hindered by the resources available at the accident locale, with specialist equipment including observation aircraft not arriving until several days after the event. Current observation solutions include satellites with Synthetic Aperture Radar (SAR) or other spectrum sensors and sensor-equipped vehicles although only aircraft or helicopters have the range and speed necessary to observe a large marine area quickly.

Satellite data availability is limited to first responders and the most frequent sensor, SAR, is incapable of measuring oil thickness (Fingas and Brown, 2014) and the complex interplay between oil thickness, viscosity and wave parameters (Zhang et al., 2015) result in further uncertainty in measurement results. SAR is unreliable in calm or rough seas (wind speeds less than 3m/s or greater than 10m/s) and environmental phenomena can produce false

positives (Topouzelis and Singha, 2016). Plausible incident sites must be verified by direct observation, usually meaning aerial observation.

However, due to remoteness, flyovers are often conducted using local aircraft with no specialist sensors or tools and crewed by a human observer (ITOPF, 2014). In extreme locations aerial observations are hampered by a lack of runways, requiring the chartering of vessels equipped with a helicopter pad, delaying observation by days, if-not weeks (Laruelle, 2011). The expense of aircraft limits their number and hence the availability of simultaneous viewpoints or constant coverage during pilot/refuel breaks. Furthermore, health and safety concerns for the crew can limit their night-time deployment and their flight route is often pre-determined before take-off, with changes at the discretion of safety and airspace concerns. Observation aircraft plan routes as ladder search patterns in the supposed direction of wreckage or oil migration, with their data relayed back to model operators that correct oil locations manually. Despite their problems, aircraft offer excellent spatial and temporal resolution in their data and are exceptionally useful when directed by an oil drift model.

Supporting tools, such as oil models, may not be available (due to a lack of data or resource allocation) in the crucial first few days following an incident. Existing models results provide useful data for response planning, but can require considerable time to do so, owing to their high complexity. However, despite their supposed accuracy, such model predictions still have to be verified by observation before resource allocation can commence (ITOPF, 2014).

*This document is a result of a research project funded by the University of Sheffield, the Engineering and Physical Sciences Research Council (EPSRC) UK and Andrew Moore & Associates Ltd.

*Corresponding author. Tel.: +447510 168575.

Email address: zhodgson1@sheffield.ac.uk (Zak Hodgson)

The advent of increasingly low-cost autonomous platforms such as unmanned aerial vehicles (UAVs) and unmanned surface vehicles (USVs) offers the potential to sample an oil spill in a more rapid fashion and in greater number than the conventional methods listed above. However, what is currently lacking is the autonomy to direct such sensor platforms to the best spatial locations for sampling the spill, for the purpose of estimating its spatial extent. It is the opinion of the authors that such autonomy should be based upon a model that incorporates the key physical processes by which oil spreads upon the ocean surface, and that such a model should be ‘lean’ in order to facilitate fast predictions for the purposes of real-time data assimilation from, and subsequent issuing of guidance commands to, the mobile sensors. This paper describes the development of such a model, henceforth named the Sheffield Combined Environment Model (SCEM).

A recent review of oil spill modelling (Spaulding, 2017) covers OSCAR (Reed et al., 2000), SIMAP/OILMAP (French McCay et al., 2016), GNOME/ADIOS (Lehr et al., 2002), though other notables in the field include the model MEDSLIK (De Dominicis et al., 2013a) and work in support of hydrodynamic models.

The review affirms modern oil spill models are complex amalgamations of Lagrangian (particle based) transport processes and varied algorithm types (stochastic and deterministic) of other processes, such as entrainment in the water column, or evaporation. There are some exceptions that use an Eulerian approach (Taylor et al., 2003), but these are more limited in scope since supporting algorithms (such as entrainment) are Lagrangian based (Wang and Shen, 2010), providing solutions per particle. State of the art 3D models aim to provide the most accurate estimations possible of oil position/properties, both surface and sub-surface, at the expense of computational speed, over an extended period of time (weeks to months of prediction) and hence include weathering effects. Inputs to the models, including geographical, wind and water current data, all come from exterior hydrodynamic models, that also vary in approach.

Environmental models provide the oil spill model with wind, wave and current velocity data. Modern 3D models commonly use a harmonic water-level tide model for boundary in-flows and out-flows and base their physical processes and turbulence closure on the work of Mellor (Mellor and Tetsuji, 1982), (Mellor, 2003). This includes 3D Navier Stokes, radiation stress from linear surface waves and a Smagorinsky eddy parameterization, but with differing discrete solution methods such as an unstructured mesh (Wang and Shen, 2010). Continuing work enabled coupling the wave model with an ocean model, and modification to incorporate depth-induced wave-breaking and wave-current interaction (Mellor, Donelan, and Oey, 2008). Wave models are still external to the ocean model in most cases (Spaulding, 2017), with the notable exception of Mellor’s continuing research, a joining of the Stevens Institute of Technology Estuarine and Coastal Ocean Model

(sECOM) and Mellor-Donelan-Oey (MDO) wave model (Marsooli et al., 2017). Some work omits Ekman currents completely (slow forming horizontal net water currents due to the force balance between the coriolis effect and wind shear), others prefer to account for them (instantaneously forming) in their oil drift angle formulation (De Dominicis et al., 2013a), while others include them in their 3D hydrodynamic model by including a coriolis force term in the Navier-Stokes equations (Marsooli et al., 2017). For SCEM, consideration was given to utilisation of the Regional Ocean Modelling System (ROMS) (Moore et al., 2011) but it was decided overly complex given the focus of SCEM on model-guided sensing rather than long term predictions.

Due to constraints on computation, communication and time, the current 3D hydrodynamic models are unsuitable for sensor guidance applications. For example, a state of the art 3D model can take 74 hours to solve a 9 day simulation across 66000 nodes (the most useful measure of area), or approximately 400km x 300km, on an 8 CPU OpenMP computer (Marsooli, 2017). By contrast, for the purposes of rapidly mapping a spill in the *immediate aftermath* of a spill, a model need only make accurate predictions a few hours ahead, hence reducing the need for high complexity. This required complexity can be further lowered if the model predictions are continually corrected using repeated re-calculation based upon the most recent sensor information; a well-established technique known as ‘state-estimation’ within the control systems community. Table 1 displays a summary of oil models, their internal environment models, intended prediction horizon and computation time. This shows the modelling gap that motivated the development of the SCEM model that prioritises speed of prediction over long-term forecast accuracy.

The separation of Ocean modelling to Oil modelling does have advantages, allowing for differing hydrodynamic approaches to be used and the appropriation of data from any source, be it small scale Boussinesq models (Lonin, 1999), large scale circulation models (Marsooli et al., 2017) or broad-scale measurements from high-frequency radar, synthetic aperture radar (SAR), wave buoys or other data sources. Furthermore, certain parameters may only need to be calculated where oil is likely to be. Wave spectra for example, could be calculated only where required. However, there are disadvantages in model separation. If the models are not integrated, or run at the same time-steps, large data-sets must be produced and stored by the hydrodynamic model for use by the oil model, which may need to interpolate the data. Also, there can be no two-way coupling between oil and hydrodynamics; the dampening effect of oil on surface waves (integral to SAR measurement) (Zhang et al., 2015) cannot be included if the hydrodynamics are pre-calculated.

In most cases, the majority of oil volume is contained on the surface, in dark slicks (ITOPF, 2011), with only 10% in the water column after 24 hours (Proctor, Flather, and Elliott, 1994). When subsumed underwater temporarily,

Oil Model	Internal Environment Model Complexity					Oil Model Complexity					Prediction Horizon					Prediction Computation Time
	External data only	Ocean surface + Wind	Wave surface dynamics	Subsurface ocean dynamics	Coupled environment and oil dynamics	Advection + Constant diffusion	Variable diffusion	Mechanical spreading	Subsurface dynamics	Oil weathering	Several hours surface drift	Half day drift	Day drift with oil separation	Long term drift with weathering		
GNOME	X					X		X		X	X				Seconds-Minutes	
SCEM	X	X	X	X		X	X	X	X		X	X			Seconds-Minutes	
MOTHY	X	X				X	X	X	X	X	X	X	X	X	Minutes-Hours	
MEDSLIK	X					X	X	X	X	X	X	X	X	X	Minutes-Hours	
POSEIDON	X	X	X			X	X	X	X	X	X	X	X	X	Minutes-Hours	
sECOM-MDO	X	X	X	X	X	X	X	X	X	X	X	X	X	X	Days	

Table 1: A qualitative summary of the features and use of several oil models. MEDSLIK, POSEIDON and MOTHY form part of the Mediterranean Decision Support System for Marine Safety and demonstrate their focus on accurate prediction of a spill, but are unsuitable for fast in-the-loop sensor guidance. SCEM displays a use of an internal environment model to supplement external data, the core short-term oil drift dynamics and prediction horizon combined with a short computation time.

depths rarely exceed 10m even in high wind conditions (Li, Zhu, and Wang, 2013). This suggests a 2D current simulation, with empirical formula induced variation in depth, a 2D wind simulation and a surface wave model are all sufficient for surface input data into a short-term oil model. Sensitivity studies of a similar model (De Dominicis et al., 2013b) demonstrate that a calibrated model retains predictive accuracy for approximately 1-2.5 days, with the forecast accuracy largely dependent upon the input ocean currents. This is sufficient for a prediction horizon of a few hours to a day, for the purpose of model-based sensor guidance.

The novelty of the work herein is the development of a joint model of the hydrodynamics and oil that is computationally efficient for model based guidance. The hydrodynamic model resolves input ocean and wind flow around local bathymetry and geography features too small to be included in the input data. A complete vertical velocity profile is calculated to the sea-bed, using tidal current, Ekman current estimates, Stokes drift and wind induced surface shear. Additionally, a complete wave spectrum is calculated where oil particles are present and environment conditions are contained within each grid cell. Use of spatio-temporally varying external data is also supported if available. The vertical velocity profile is important to estimate the further dispersal of oil resulting from its subsurface and resurfacing within water, without utilising time-intensive 3D flow simulation or large 3D external data-sets that may be unavailable for the local region.

The oil model within SCEM integrates a number of validated algorithms from prior work, with small modifications such as a random walk diffusion correction (Hunter, Craig, and Phillips, 1993). The internal hydrodynamic model makes the model suitable for use in regions where high-fidelity external data is absent and can supplement external data by resolving flow around local bathymetry or correcting flow with sensor data. Combined with the contained oil dynamics a complete system is available for analysis and control of sensors, providing a prediction over a short-time horizon (several hours) with prediction error reduced through live sensor information.

2. Internal Environment Model

The environment model contains interconnected sub-systems that describe large scale ocean currents, local currents, local wind and local wave conditions. Figure 1 shows the main physics sub-components and their interactions.

At each time-step the local wind field is calculated first, followed by the large scale ocean current velocity field, then the depth velocity profiles are calculated and finally the wave model is updated to produce a wave induced velocity. These are used, together with oil-only effects such as turbulent diffusion, mechanical spreading, entrainment and buoyancy, to move oil particles. The complete forward simulation algorithm is described in pseudocode in Algorithm 1.

2.1. Grid structure

The spatial computation domain is denoted $\Omega \subset \mathbb{R}^3$, selecting a cuboid section of the Earth including land and ocean with depth. The upper surface $\delta\Omega \subset \mathbb{R}^2$ of the domain (the water/land to air interface) is discretised upon a regularly spaced grid of n_x grid cells (west to east) and n_y cells (south to north), with equal spacing δx and δy in the respective directions. Each surface grid-cell represents a Cartesian coordinate volume of $\delta x \delta y \bar{z}_{ij}$, where $[0, \bar{z}_{ij}]$ is the closed interval of water depth in that cell and $\bar{z}_{ij} := \bar{z}_{ij}(x_i, y_j) : \delta\Omega \rightarrow \mathbb{R}_+$ is the average total water depth in that cell area. The set of positive real numbers including 0 is defined by $\mathbb{R}_+ \subset \mathbb{R}$. A grid cell at indexed position (x_i, y_j) covers the Cartesian coordinate positions: $(x \pm \frac{\delta x}{2}, y \pm \frac{\delta y}{2}, [0, \bar{z}_{ij}])$, where x_i represents the west to east horizontal grid index, y_j is the south to north grid index.

Subsurface water is discretised with a two stage fine and coarse mesh, such that for each grid cell there exists a set of depths $\mathbf{z}(x_i, y_j)$, defined by $\mathbf{z}(x_i, y_j) = \{0, \delta z_1, 2\delta z_1, \dots, N_{\text{crit}}\delta z_1, z_{\text{crit}}, z_{\text{crit}} + \delta z_2, z_{\text{crit}} + 2\delta z_2, \dots, N_{\bar{z}_{ij}}\delta z_2\}$. Depth spacings δz_1 and δz_2 are the finer and coarser vertical grid spacing respectively, $N_{\text{crit}} \in \mathbb{N}$ is the number of fine mesh grid cells. The switch depth from fine to coarse mesh, z_{crit} , is determined by the maximum depth of oil particle insertion into the water column (explained in Section 3.2), or specified by the user. By utilising a two stage depth grid, finer detail can be maintained near the surface where the majority of contaminant mechanics take place. A 3D grid cell is specified by the indexes (x_i, y_j, z_w) , where z_w is the surface to sea floor grid index.

2.1.1. Model States

Each grid-cell is defined by its geo-spatial coordinates and contains the following states:

- Environmental information (temperature, water density etc).
- Wave spectra.
- Current time wind velocity.
- Previous 12-hour mean wind velocity.
- Tidal flow velocity profile.
- Wind induced surface shear flow velocity profile.
- Ekman current velocity profile.
- Stokes drift velocity profile.

The states are formally defined in the following subsections.

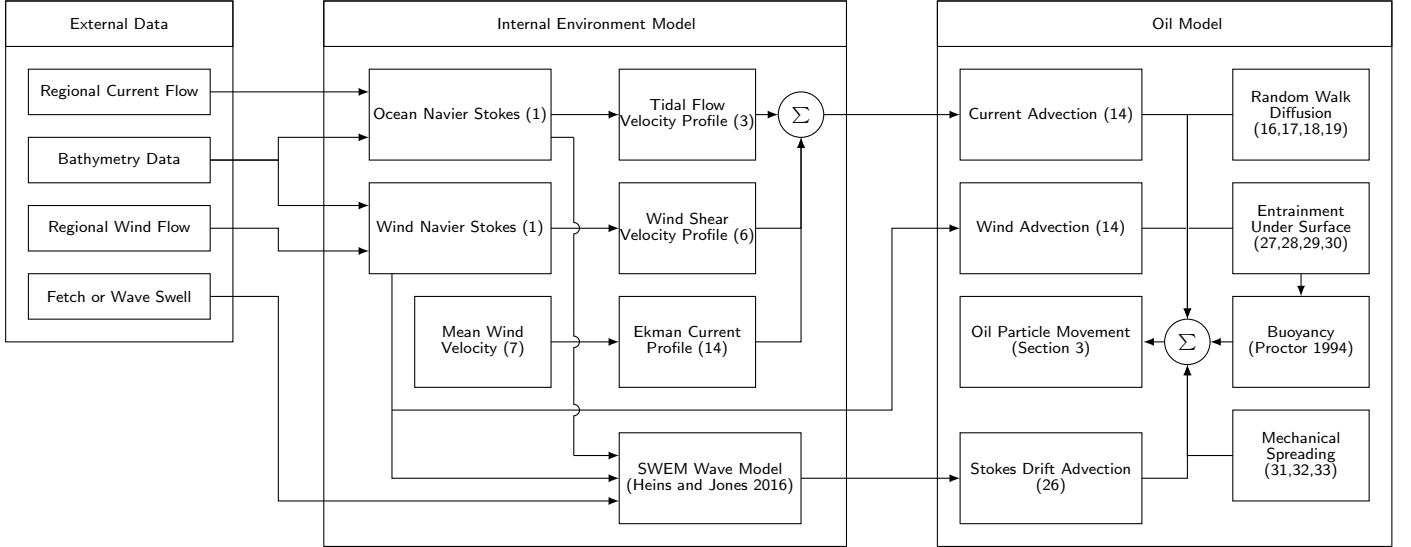


Figure 1: A block diagram of the fluid model, showing the initialisation with external data and the coupling between wind, current and wave motion in producing a contaminant velocity field.

2.2. Flow solver

A 2D Navier Stokes solver has been implemented to determine local flow velocities for both wind and water, using assumed, measured or external model-provided boundary data. The general form of the Navier Stokes equations, assuming 2-dimensional incompressible flow is:

$$\frac{\delta \vec{U}}{\delta t} = -(\vec{U} \cdot \nabla) \vec{U} + \nu \nabla^2 \vec{U} - \nabla p + \vec{s}_u, \quad (1a)$$

$$\nabla \cdot \vec{U} = 0, \quad (1b)$$

where $\vec{U}(x, y, z, t) : \Omega \times \mathbb{R}_+ \rightarrow \mathbb{R}^2$ is the in-plane velocity field such that $U(x, y, z, t) = [u(x, y, z, t), v(x, y, z, t)]^T$, with $u(x, y, z, t)$ and $v(x, y, z, t)$ the in-plane velocity components in the west to east and south to north directions respectively. For notational brevity the space and time dependency of these variables is not shown in the equations above and similarly throughout the remainder of this paper. In addition $t \in \mathbb{R}_+$ is time, $\nu \in \mathbb{R}$ is the kinematic viscosity of the fluid, $p(x, y, t) : \delta\Omega \times \mathbb{R}_+ \rightarrow \mathbb{R}$ is the surface internal pressure field and $\vec{s}_u := \vec{s}_u(x, y, t) : d\Omega \times \mathbb{R}_+ \rightarrow \mathbb{R}^2$ are external surface forces, if present. For wind flow $\vec{U} := \vec{U}_w = [u_w, v_w]^T$, for current flow $\vec{U} := \vec{U}_c = [u_c, v_c]^T$ and for Ekman wind $\vec{U} := \vec{U}_E = [u_E, v_E]^T$. Flow is calculated for ocean surface currents and for wind velocities at 10m above sea level by solving (1) subject to initial conditions on velocity at the simulation start time. These are set from external data, or by setting $\vec{U}(x, y, z, 0)$ to a best-estimate of mean flow if no data is available. Boundary conditions are described in the next section.

The Navier-Stokes equations are spatially discretised upon a staggered grid (F. Harlow and J. Welch, 1965), with spatial derivatives approximated by finite differences. With respect to time-stepping, diffusion terms are solved

using a backward Euler method and Gauss Seidel Successive Over Relaxation (Stam, 2001), whilst advective terms are solved using a forward Euler method. Mass conservation is enforced via an iterative pressure projection step, in which the pressure field is found using Gauss-Seidel Successive Over Relaxation (Stam, 2001), with subsequent correction of the velocity field. This is repeated until the flow-field divergence is below a nominal tolerance. The time-step is variable with the step size determined by the Courant number (Courant, Friedrichs, and Lewy, 1967)

2.2.1. Boundaries, measurements and obstacles

Obstacles are regions of $\vec{U}_c = 0$ for ocean current flow velocity, or $\vec{U}_w : \|\vec{U}_w\|_2 \leq \kappa^2 \|\vec{U}_{w,max}\|_2$ for wind flow where $\kappa := \kappa(x, y) : \delta\Omega \rightarrow \mathbb{R}_+$ is a wind resistance coefficient based on the environment and $\vec{U}_{w,max}$ the maximum wind velocity. The presence of obstacles, such as coastline geography, is accounted for by the use of Dirichlet boundary conditions on the velocity field in relevant grid cells. Due to the staggered grid implementation, this is a form of semi-slip boundary (F. Harlow and J. Welch, 1965). This is not unprecedented in ocean models, a user selected value for slip is found in the NEMO ocean model (Madec, 2011), with large scale models using free-slip and small-scale models using no-slip. A semi-slip induces the circulation expected from boundary layers but avoids under-estimation of fluid velocities in sparse grids near walls.

Velocity field information from measurements or external data can either be set precisely or within a bounded range, between a minimum and maximum value, representing the accuracy of the sensor. The measured value of an uncertain measurement is applied prior to the projection step of flow calculation. During pressure projection the value is altered, within the bounded range, to ensure

divergence free flow. If the value is at a boundary limit, or is assumed accurate (a recent measurement), then it is fixed during pressure projection and other free flow-field velocities are adjusted by the pressure field until the flow is divergence free.

Domain edge boundary conditions can be specified as Dirichlet conditions on velocity, or left open as free-flow.

2.3. Wind flow

Calculation of wind velocity \vec{U}_w is handled by the flow solver described in Section 2.2, with the replacement of zero flow boundaries for obstacles by maximum wind-speed conditions to represent wind resistant areas such as cities or mountains. This acts as a flow restriction and thus resolves flow to greater accuracy for local geographic features. The velocity limit $\vec{U}_{wlim} := \vec{U}_{wlim}(x, y) : \delta\Omega \rightarrow \mathbb{R}^2$ is calculated by the urban canopy profile

$$\vec{U}_{wlim} = (1 - \lambda_p)^2 \left\| \vec{U}_{wmax} \right\|_2, \quad (2)$$

where $\lambda_p := \lambda_p(x, y) : \delta\Omega \rightarrow [0, 1] \subset \mathbb{R}$ is the obstruction plan, or footprint, density in the cell area at 10m altitude (CERC, 2017). If an obstruction density map is not available, a coefficient can be specified in place of $(1 - \lambda_p)^2$ for all coastal and land cells.

2.4. Ocean flow

The Navier-Stokes equation are solved in 2D, but a depth velocity profile is important in calculating oil-trajectories and inducing the separation of slicks caused by sub-surface shear flows and entrainment. Typical individual velocity profiles are shown in Figure 2.

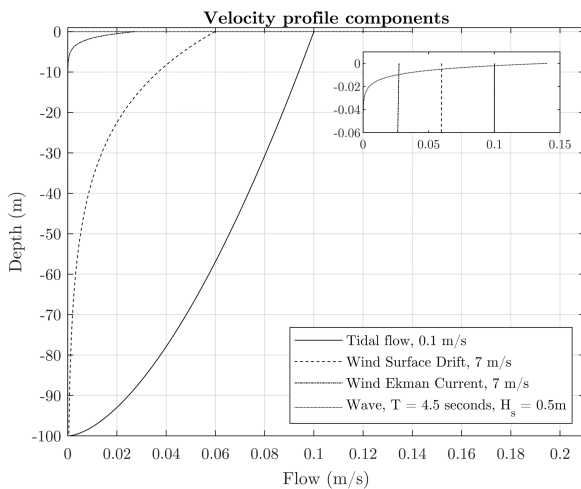


Figure 2: A depiction of sub-surface flow resulting from mechanisms included in the three-dimensional model. The insert magnifies the sub-surface flow at shallow depths, note the very shallow effect of wind surface drift.

2.4.1. Tidal and circulation flow

The velocity profile, introducing vertical variation to \vec{U}_c for a tide driven flow, follows a standard logarithmic profile where $z \in [0, \bar{z}] \subset \mathbb{R}$ is depth in the water column, with $z = 0$ at the surface and $z = \bar{z}$ at maximum water depth where \bar{z} is the mean total water depth in that cell area as in section 2.1. A no-slip condition, $\vec{U}_{c_z} = 0$ is imposed on the sea floor and \vec{U}_{c_z} increases to its maximum value at the surface. As predictions focus on surface oil particles, boundary layer simulation is omitted and U_{c_z} can be simply defined as (Thiébaud and Sentchev, 2016)

$$\vec{U}_{c_z} = \vec{U}_{c_0} \left(1 - \frac{z}{\bar{z}}\right)^{\frac{1}{6}}, \quad (3)$$

where the empirical denominator parameter in the power law has been assigned the value of 6, which falls in the range of accepted values for ebbing and flowing tides.

2.4.2. Wind induced surface shear

Under strong wind conditions the velocity of surface water is heavily affected by the boundary stress between the two-phase flow of air and water, so is vital for inclusion in an advective ocean model. Large scale models often use measured wind speed data (De Dominicis et al., 2013a) or wind speed estimated from surface roughness (measured via radar scattering) (Smith, 1988) to simply calculate a surface flow velocity. This takes the form of a scaled velocity $\alpha_w \left\| \vec{U}_w \right\|_2$, rotated by a wind drift angle $\beta := \beta(x, y, t) : \delta\Omega \times \mathbb{R}_+ \rightarrow \mathbb{R}$, representing the balancing of wind shear and coriolis effects. This velocity is then scaled to a logarithmic velocity profile (Wu, 1975), modelled in oceans as beginning at z_0 (the wind driven surface layer) and falling to zero effect at z_c meters (Proctor, Flather, and Elliott, 1994). This latter depth can be approximated as

$$z_c \approx \alpha_z L. \quad (4)$$

A value of $\alpha_z = 2$ is suggested to give good agreement with observations (Elliott, 1986) in a short-fetch environment, using L as the dominant wavelength of sea-surface waves. For even a low wind speed fetch in deep water, wave lengths are likely to be around 8 meters giving rise to large z_c values and a large effect of wind on sub-surface currents, with data supporting a wind penetration depth of 40m (Elliott, 1986).

An assumption of the above method is instantaneous changes of sub-surface currents in response to local wind gusting. Here, wind effects are modelled in parts, deep effects are modelled as a combination of slow time-varying Ekman currents and stokes drift from a linear wave model. Shallow effects are instantaneously applied by a logarithmic velocity profile. In a wind wave spectrum, local wind affects only the small-scale ripples (capillary waves) and gravity-wind waves that are accounted for in the linear wave model. Modelling just capillary waves gives rise to

varying surface roughness (as wave amplitude) across wind conditions, of typical wavelength (Lamb, 1895) defined by

$$L_{\text{capillary}} = 2\pi \sqrt{\frac{\sigma_{\text{water}}}{(\rho_{\text{water}} - \rho_{\text{air}})g}}, \quad (5)$$

where for an air-water interface, $L_{\text{capillary}} = 0.017\text{m}$ (Lamb, 1895) and σ_{water} is the surface tension of water, ρ_{water} and ρ_{air} are the densities of water and air, respectively. Thus the new wind shear zero effect depth for $\alpha_z = 2$ is 0.037m when using (5) to determine the wavelength in 4. This is a shallow depth, where viscous shear and vertical mixing allows an assumption of a velocity change time-scale much smaller than the simulation time-step. Hence velocity changes immediately with fluctuating wind as in traditional percentage based algorithms for surface oil spill drift due to wind/wave interaction (Spaulding, 2017), with the wind shear velocity profile $\vec{U}_{w_z} := \vec{U}_{w_z}(x, y, z, t) : \Omega \times \mathbb{R}_+ \rightarrow \mathbb{R}^2$, defined by

$$\vec{U}_{w_z} = \alpha_w \vec{U}_w e^{-\frac{2\pi}{z_c} z}, \quad (6)$$

where $\alpha_w \in [0.005, 0.03] \subset \mathbb{R}$. A value of 0.02 is suggested for α_w (Proctor, Flather, and Elliott, 1994), but varies within literature (Kim et al., 2014).

2.4.3. Ekman currents

Ekman currents describe the net motion of fluid that results from the balance of a forcing wind, turbulent drag and Coriolis forces. In a small scale simulation it would be preferable not to assume an instantaneous (in distance and time) change in the sub-surface layer velocity due to wind. Ekman currents take approximately 12 hours to form ($T_E = 12$ hours), accelerating approximately linearly to their fully formed magnitude (Weatherly, 1975). Ideally, the Ekman current would change towards its final value at each time-step, but this would require changing every depth value in every grid cell, at every time-step, leading to excessive computational load. An alternative would be to keep a moving average of the last 12 hours of wind data, but this requires stored data and introduces a large phase lag in Ekman changes. For a domain where wind-speed changes are frequent, an incremental weighted mean of wind speeds to form an average of the past 12 hours of wind speed is proposed. The Ekman wind velocity $\vec{U}_{w_E} := \vec{U}_{w_E}(x, y, t) : \delta\Omega \times \mathbb{R}_+ \rightarrow \mathbb{R}^2$, is calculated for the surface of each grid cell:

$$\vec{U}_{w_E} = \frac{W_{E_1} \vec{U}_{w_E}^{t-\delta t} + W_{E_2} \vec{U}_w^t}{W_{E_1} + W_{E_2}}, \quad (7)$$

where the Ekman averaged wind velocity at the previous time-step is $\vec{U}_{w_E}^{t-\delta t}$ and \vec{U}_w^t is the current time wind-velocity. The weights for the value $W_{E_1} \in \mathbb{R} : 0 \leq W_{E_1} \leq 1$ and future values $W_{E_2} \in \mathbb{R} : 0 \leq W_{E_2} \leq 1$ are calculated as

$$W_{E_1} = \frac{T_E - \delta t}{\frac{1}{2}T_E} \quad (8a)$$

and

$$W_{E_2} = \frac{\delta t}{T_E}. \quad (8b)$$

Figure 3 shows the growth and decay of the Ekman wind speed, used to calculate the Ekman current, under a range of wind conditions when calculated by both the weighted mean and moving average approaches. Results from literature suggest there should be no lag between wind stress and Ekman shelf velocities (Kirincich and Barth, 2008). Whilst both approaches induce a lag in the Ekman current velocity, inspection of Figure 3 clearly shows the lag from the moving average approach is significantly greater than that from the weighted mean approach, to the point where the Ekman wind speed response is almost completely out of phase with the forcing wind.

The wind stress of the surface layer can be used to estimate the Ekman current magnitude. Prior work provides stress coefficients for water under a variety of conditions, including adjustment factors for wind speeds measured at various heights to normalise their values at 10m above sea level (Wu, 1980) and (Smith, 1988). Let the stress coefficient $C_{D_{\text{stress}}} := C_{D_{\text{stress}}}(x, y, t, \|\vec{U}_{w_E}\|_2) : \delta\Omega \times \mathbb{R}_+ \times \mathbb{R} \rightarrow \mathbb{R}_+$. Hence, using \vec{U}_{w_E} as wind velocity yields

$$\tau = C_{D_{\text{stress}}} \rho_{\text{air}} \|\vec{U}_{w_E}\|_2^2, \quad (9)$$

where the scalars $\tau := \tau(x, y, t) : \delta\Omega \times \mathbb{R}_+ \in \mathbb{R}_+$ are the wind stresses on the water surface and $\rho_{\text{air}} \in \mathbb{R}_+$ is the air density. A final Ekman current velocity profile is calculated (Pond and Pickard, 2013), using a vertical eddy viscosity coefficient (Rasmussen, 1985) of $A_z := A_z(x, y, t) : \delta\Omega \times \mathbb{R}_+ \rightarrow \mathbb{R}_+$ and a surface Ekman speed $V_{0_E} := V_{0_E}(x, y, t) : \delta\Omega \times \mathbb{R}_+ \rightarrow \mathbb{R}_+$ defined by

$$A_z = 4.3 \times 10^{-4} \|\vec{U}_{w_E}\|_2^2 \quad (10a)$$

and

$$V_{0_E} = \frac{\sqrt{2}\pi\tau}{z_E \rho_{\text{water}} |f|}, \quad (10b)$$

where $z_E := z_E(x, y, z, t) : \Omega \times \mathbb{R}_+ \rightarrow \mathbb{R}_+$ is the Ekman layer depth (Pond and Pickard, 2013), $f := f(x, y, t) : \delta\Omega \times \mathbb{R}_+ \rightarrow \mathbb{R}$ is the coriolis frequency and $\rho_{\text{water}} \in \mathbb{R}_+$ is the water density. Adjusting for a coordinate system where u is positive east velocity and v is positive north, with an ascending z with depth and positive clockwise from north angles, an alternative formulation that also reflects the smaller drift divergence angle in current formations under high wind conditions can be described by

$$u_{E_z} = \pm V_{0_E} \sin\left(\beta_{\text{rad}} - \frac{\pi}{z_E} z\right) e^{-\frac{\pi}{z_E} z}, \quad (11a)$$

where the negative sign applies to the northern hemisphere, the positive to the southern hemisphere. Similarly

$$v_{E_z} = \pm V_{0_E} \cos\left(\beta_{\text{rad}} - \frac{\pi}{z_E} z\right) e^{-\frac{\pi}{z_E} z}, \quad (11b)$$

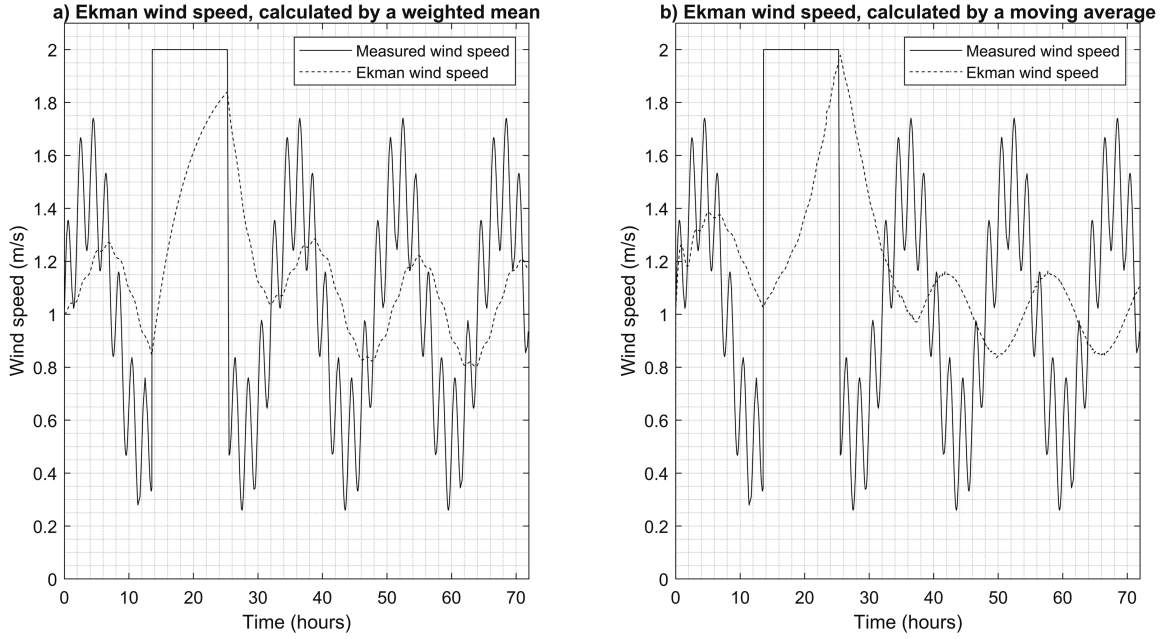


Figure 3: A depiction of the wind speed \vec{U}_w that Ekman currents are calculated from, \vec{U}_{wE} , under noisy wind conditions. a) Calculated using the weighted mean approach. b) Calculated by a traditional 12 hour moving average approach, which shows a more linear growth but significantly greater lag.

where a wind drift angle (Wang and Shen, 2010) is proposed for the Ekman current angle, instead of a constant 45 degrees:

$$\beta = \begin{cases} 40^\circ - 8^\circ \sqrt[4]{u_w^2 + v_w^2} & \text{for } 0 \leq \sqrt{u_w^2 + v_w^2} \leq 25 \text{ m/s} \\ 0^\circ & \text{for } \sqrt{u_w^2 + v_w^2} > 25 \text{ m/s} \end{cases}, \quad (12a)$$

and

$$\beta_{\text{rad}} = \beta \frac{\pi}{180}. \quad (12b)$$

The velocity components (11) compose the fully formed Ekman velocity $\vec{U}_{cEz} = [u_{Ez}, v_{Ez}]^T$, where $\vec{U}_{cEz} := \vec{U}_{cEz}(x, y, z, t) : \Omega \times \mathbb{R}_+ \rightarrow \mathbb{R}^2$.

These equations produce an Ekman velocity profile, shown in Figure 4, that follows a typical spiral pattern and has a magnitude of approximately 1% of the wind speed. This is as expected, the 3% wind velocity advection employed by classical models will be a composite of the smaller Ekman currents, Stokes drift and Surface stress induced currents calculated separately here.

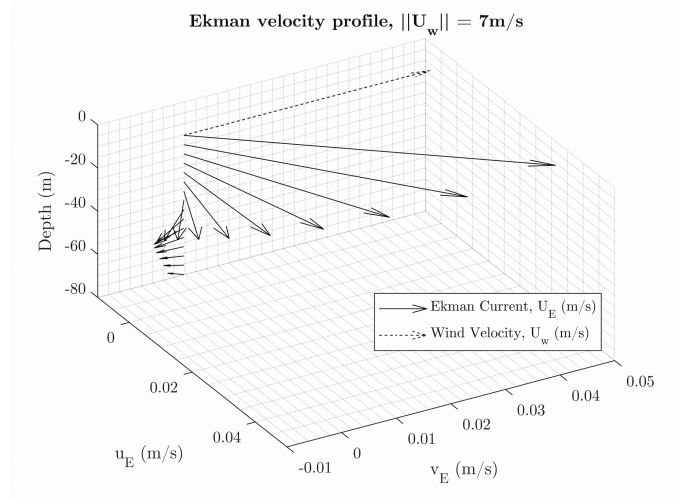


Figure 4: The spatial variation of Ekman velocity with depth resulting from non-aligned wind and current angles.

2.5. Linear wave model

To determine the effect of waves on contaminants a spatio-temporally varying wave spectrum is approximated by the Sheffield Wave Environment Model (SWEM) (Heins and Jones, 2016), which combines modified wave spectra from ocean swell, local wind, surface current and finite water depth to simulate the ocean surface. It includes a directional spreading function and swell estimation from fetch parameters or buoy data. Each cell updates its wave model with the local wind and surface cur-

rent velocity at every time-step. The wave models then re-evaluate the wave spectra, along with the significant wave height $H_s := H_s(x, y, t) : \delta\Omega \times \mathbb{R}_+ \rightarrow \mathbb{R}_+$, wavelength $L := L(x, y, t) : \delta\Omega \times \mathbb{R}_+ \rightarrow \mathbb{R}_+$ and wave period $T := T(x, y, t) : \delta\Omega \times \mathbb{R}_+ \rightarrow \mathbb{R}_+$ for each grid cell. In a time-constrained simulation, the wave model can be updated only in cells where oil is present without adversely affecting results.

3. Oil model

The oil model uses a common Lagrangian approach (Spaulding, 2017), utilising large numbers of particles (see section 3.5), each representing a volume of contaminant. Particles undergo advection and turbulent diffusion in response to forcing from the environmental model. Particles are then used to build a thickness map and undergo mechanical spreading in areas where the thickness is above a minimum value, with particle size determined from oil properties. Particles can be entrained underwater, determined by variables from the wave model, with subsequent resurfacing dependent upon vertical turbulent diffusion and terminal buoyancy velocity.

3.1. Advection and diffusion

The advective velocity of particles at depth z consists of horizontal velocity components u_{o_z} , v_{o_z} and a vertical velocity component w_{o_z} . These are determined from a summation of tidal, wind induced surface shear and Ekman current velocities, plus turbulent diffusion terms as follows:

$$\begin{aligned} \begin{bmatrix} u_{o_z} \\ v_{o_z} \\ w_{o_z} \end{bmatrix} &= \alpha_{w_o} \begin{bmatrix} u_w \\ v_w \\ 0 \end{bmatrix} + \alpha_{c_o} \begin{bmatrix} u_{c_z} \\ v_{c_z} \\ 0 \end{bmatrix} \\ &+ \begin{bmatrix} u_{w_z} \\ v_{w_z} \\ 0 \end{bmatrix} + \begin{bmatrix} u_{E_z} \\ v_{E_z} \\ 0 \end{bmatrix} + \begin{bmatrix} u_{s_z} \\ v_{s_z} \\ 0 \end{bmatrix} \\ &+ \begin{bmatrix} u_d \\ v_d \\ 0 \end{bmatrix} + \begin{bmatrix} u' \\ v' \\ w'_z \end{bmatrix}, \end{aligned} \quad (13)$$

where $\alpha_{w_o} \in \mathbb{R} : 0 \leq \alpha_{w_o} \leq 0.05$ is a coefficient for additional wind advection and $\alpha_{c_o} \in \mathbb{R} : 0.95 \leq \alpha_{c_o} \leq 1.1$ is an advection coefficient for tidal currents. The diffusion correction velocities $u_d := u_d(x, y, t, D_h) : \delta\Omega \times \mathbb{R}_+ \times \mathbb{R} \rightarrow \mathbb{R}$ and $v_d := v_d(x, y, t, D_h) : \delta\Omega \times \mathbb{R}_+ \times \mathbb{R} \rightarrow \mathbb{R}$ are defined

$$u_d(x, y, t, D_h) = \frac{\delta D_h}{\delta x}, \quad (14a)$$

in the horizontal x direction and

$$v_d(x, y, t, D_h) = \frac{\delta D_h}{\delta y} \quad (14b)$$

in the horizontal y direction. They are the spatial derivative of $D_h := D_h(x, y, t) : \delta\Omega \times \mathbb{R}_+ \rightarrow \mathbb{R}$, the horizontal diffusion coefficient (Hunter, Craig, and Phillips,

1993). The turbulent diffusion velocities comprise of $u' := u'(x, y, t) : \delta\Omega \times \mathbb{R}_+ \in \mathbb{R}$, $v' := v'(x, y, t) : \delta\Omega \times \mathbb{R}_+ \in \mathbb{R}$, $w' := w'(x, y, z, t) : \Omega \times \mathbb{R}_+ \in \mathbb{R}$ in the horizontal x and y plane and vertical z direction respectively. The Stokes drift velocities (defined in Section 3.1.1) $u_{sz} := u_{sz}(x, y, z, t) : \Omega \times \mathbb{R}_+ \in \mathbb{R}$, $v_{sz} := v_{sz}(x, y, z, t) : \Omega \times \mathbb{R}_+ \in \mathbb{R}$ in the x and y horizontal direction respectively. The additional wind advection represents only the carrying of oil droplets by wind, since the major wind drift is accounted for in the hydrodynamic model.

Turbulent diffusion is calculated by the common random walk method (Spaulding, 2017), but avoids direct parameter setting for horizontal diffusivity and vertical diffusivity coefficients in favour of empirical formulae that also introduce variation in the diffusion coefficient dependent upon flow properties. Spatial variation in diffusion coefficient results in a requirement for a diffusion correction velocity (Hunter, Craig, and Phillips, 1993). Horizontal turbulent diffusion velocity is assumed constant with depth and calculated (Chao, Shankar, and Wang, 2003) using:

$$u' = \xi \sqrt{\frac{12D_h}{\delta t}} \sin(2\pi\phi), \quad (15a)$$

$$v' = \xi \sqrt{\frac{12D_h}{\delta t}} \cos(2\pi\phi), \quad (15b)$$

where ξ and ϕ are particle specific random variables with uniform distribution in $[0, 1]$. Vertical turbulent diffusion velocity is depth dependent and calculated (Lardner and Gunay, 2000) according to:

$$w' = (2\zeta - 1) \sqrt{\frac{6D_{v_z}}{\delta t}}, \quad (16)$$

where ζ is a particle specific random variable with uniform distribution in $[0, 1]$. Coefficients for horizontal diffusivity D_h (Baldauf and Zängl, 2012) and vertical diffusivity $D_{v_z} := D_{v_z}(x, y, t) : \delta\Omega \times \mathbb{R}_+ \rightarrow \mathbb{R}_+$ (Li, Zhu, and Wang, 2013) are calculated as follows:

$$D_h = \frac{c_{smag}}{\frac{1}{\delta x^2 + \delta y^2}} \sqrt{T_{smag}^2 + S_{smag}}, \quad (17a)$$

$$T_{smag} = \frac{\delta u_c}{\delta x} - \frac{\delta v_c}{\delta y}, \quad (17b)$$

$$S_{smag} = \frac{\delta u_c}{\delta y} + \frac{\delta v_c}{\delta x}, \quad (17c)$$

$$D_{v_z} = 0.028 \frac{H_s^2}{T} e^{-2\frac{z}{L}}, \quad (17d)$$

where $c_{smag} \in \mathbb{R} : 0.01 \leq c_{smag} \leq 0.3$ is an empirical coefficient, with a nominal default value of 0.1.

3.1.1. Stokes Drift

Stokes drift is the net horizontal movement of a particle due to wave motion, resulting from shear stresses and mixing layers from surface gravity waves. For each grid cell in which there are oil particles and for each time-step, the spectral wave model SWEM is used to compute the wave parameters that govern Stokes drift, chiefly significant wave height H_s , wavelength L and wave period T . These are evaluated from the peak magnitude $a_p := a_p(x, y, t) : \delta\Omega \times \mathbb{R}_+ \rightarrow \mathbb{R}_+$ and corresponding peak frequency $f_p := f_p(x, y, t) : \delta\Omega \times \mathbb{R}_+ \rightarrow \mathbb{R}_+$ of the wave spectrum.

Webb proposes the use of the peak frequency, with a Stokes drift amplitude modified by the spectral moment (calculated through intergrands) and empirical terms specific to that spectrum (Webb and Fox-Kemper, 2011). SWEM's spectrum is a summation of several others and therefore this approach would require multiple calculations of spectral moments and ultimately, too much computation. Hence, only the peak information of the SWEM spectrum (representing the fetch, local current and local wind interaction) is used, as the high frequency ripple waves are accounted for through wind shear.

Stokes drift magnitude is similar to a near-surface tidal shear (Elliott, 1986) or 1 - 2% of the wind speed (Proctor, Flather, and Elliott, 1994). The literature suggested (Elliott, 1986) hyperbolic trigonometric formulation of Stokes drift can become undefined in deep water conditions, hence it is redefined to give the Stokes drift speed:

$$\left\| \vec{U}_{s_z} \right\|_2 = \omega k a_p^2 e^{-2kz}, \quad (18)$$

where $\omega = 2\pi/T_{\text{peak}}$, $k = 2\pi/L_{\text{peak}}$ using the wave spectrum peak values from SWEM. To achieve an accurate Stokes drift velocity, the wave spectrum produces an average wave energy direction and scales the Stokes drift velocity to the proportion of wave energy in that direction compared to the total wave energy in the spectrum. The direction and magnitudes of the waves are expressed in polar coordinates as follows:

$$\theta_{\Psi_{\text{Total}_i}} = \text{atan2} \left(\frac{k_y}{k_x} \right), \quad (19a)$$

$$r_{\Psi_{\text{Total}_i}} = \Psi_{\text{Total}}(k_x, k_y), \quad (19b)$$

where $\Psi_{\text{Total}}(k_x, k_y) := \Psi_{\text{Total}}(k_x(x, y, t), k_y(x, y, t)) : \delta\Omega \times \mathbb{R}_+ \rightarrow \mathbb{R}_+$ is the energy of the waves with wavenumbers $k_x := k_x(x, y, t) : \delta\Omega \times \mathbb{R}_+ \rightarrow \mathbb{R}$ and $k_y := k_y(x, y, t) : \delta\Omega \times \mathbb{R}_+ \rightarrow \mathbb{R}$. The polar angle $\theta_{\Psi_{\text{Total}_i}} := \theta_{\Psi_{\text{Total}_i}}(x, y, t) : \delta\Omega \times \mathbb{R}_+ \rightarrow \mathbb{R}$ and magnitude $r_{\Psi_{\text{Total}_i}} := r_{\Psi_{\text{Total}_i}}(x, y, t) : \delta\Omega \times \mathbb{R}_+ \rightarrow \mathbb{R}_+$ form the polar coordinate representation of that wave-number, with magnitude being the wave energy and angle as the wave direction. The wave spectrum is thus converted from 2D $[k_x, k_y]$ wave numbers to a $k_x k_y$ by 1 vector of polar coordinates. The sum of the vector of polar coordinates provides an average wave energy polar

coordinate with magnitude and direction of the average wave energy:

$$[\theta_{\text{sum}}, r_{\text{sum}}] = \sum_{i=1}^{k_x k_y} [\theta_{\Psi_{\text{Total}_i}}, r_{\Psi_{\text{Total}_i}}], \quad (20a)$$

$$\Psi_{\text{avg}_\theta} = r_{\text{sum}}. \quad (20b)$$

The polar angle $\theta_{\text{sum}} := \theta_{\text{sum}}(x, y, t) : \delta\Omega \times \mathbb{R}_+ \rightarrow \mathbb{R}$ and magnitude $r_{\text{sum}} := r_{\text{sum}}(x, y, t) : \delta\Omega \times \mathbb{R}_+ \rightarrow \mathbb{R}_+$ form the polar coordinate with magnitude and direction equivalent to the average wave energy. This wave energy magnitude $\Psi_{\text{avg}_\theta} := \Psi_{\text{avg}_\theta}(x, y, t) : \delta\Omega \times \mathbb{R}_+ \rightarrow \mathbb{R}$ is used to attenuate stokes drift velocity by the fraction of wave energy that is in the average wave direction $\Psi_{fr} := \Psi_{fr}(x, y, t) : \delta\Omega \times \mathbb{R}_+ \rightarrow \mathbb{R}$, calculated by

$$\Psi_{fr} = \frac{\Psi_{\text{avg}_\theta}}{\sum_{i=1}^{k_x k_y} \Psi_{\text{Total}_i}(k_x, k_y)}. \quad (21)$$

Stokes drift speed $\left\| \vec{U}_{s_z} \right\|_2$ is in the direction of Ψ_{avg_θ} , where $\vec{U}_{s_z} : \Omega \times \mathbb{R}_+ \rightarrow \mathbb{R}^3$ is the stokes drift velocity vector $\vec{U}_{s_z} = [u_{s_z}, v_{s_z}, 0]^T$, forming a stokes drift velocity:

$$\vec{U}_{s_z} = \omega k a_p^2 e^{-2kz} \Psi_{fr}. \quad (22)$$

3.2. Entrainment and buoyancy

Oil entrainment from the surface slick to the water column represents the movement of oil particles underwater by wave action and can be modelled as a random process with a probability for a particle to be entrained at a given time. The principle variable in the volume of oil entrained is the rate-scale scalar $\lambda_{\text{ow}} := \lambda_{\text{ow}}(x, y, t) : \delta\Omega \times \mathbb{R}_+ \rightarrow \mathbb{R}$ (Tkalich and Chan, 2002), which is defined by

$$\lambda_{\text{ow}} = \frac{\pi k_e \gamma H_s}{8\alpha T_{\text{peak}} L_{\text{ow}}}, \quad (23)$$

where $k_e \in [0.3, 0.5] \subset \mathbb{R}$ is an empirical constant, H_s is the peak significant wave height, T_{peak} is the wave period from the linear wave model and $L_{\text{ow}} \in \mathbb{R}_+$ is a vertical length scale parameter that depends on the type of breaking wave. This is valued between 10m and 20m (Tkalich and Chan, 2002). The vertical mixing term coefficient is $\alpha \in \mathbb{R} : 1.15 \leq \alpha \leq 1.85$. The parameter $\gamma := \gamma(x, y, t) : \delta\Omega \times \mathbb{R}_+ \rightarrow \mathbb{R}$ is a dimensionless damping coefficient that takes the following values:

$$\gamma = \begin{cases} 10^5 \omega E_w^{0.25}, & \text{for white-capping waves,} \\ 1.8 \times 10^{-7} \omega^3, & \text{for swell decay,} \end{cases}$$

where $E_w := E_w(x, y, t) : \delta\Omega \times \mathbb{R}_+ \rightarrow \mathbb{R}_+$ is calculated by

$$E_w = \frac{g \rho_{\text{water}} H_s^2}{16}, \quad (24)$$

where g is the gravitation acceleration constant of 9.81m/s. The probability of entrainment P_s for a Lagrangian particle for a discrete time-step $\Delta t \in \mathbb{R}$ is as follows (Wang and Shen, 2010):

$$P_s = 1 - e^{(-\lambda_{ow}\Delta t)}. \quad (25)$$

If the particle is inserted at this time-step, it enters the water column with intrusion depth:

$$D_i = (1.35 + 0.35(2\phi - 1))H_s, \quad (26)$$

where ϕ is a particle specific random variable with a uniform distribution in $[0, 1]$ (Delvigne and Sweeney, 1988). The maximum depth of intrusion, when $\phi = 1$, can be utilised as z_{crit} to ensure a high resolution grid for entrained sub-surface oil particles.

Oil particle buoyancy follows a typical scheme of instantaneous rising at a steady buoyancy velocity, determined by the oil droplet size, the water viscosity and the density difference (Proctor, Flather, and Elliott, 1994). This buoyancy velocity is added to w , the vertical component of oil particle velocity.

3.3. Thickness and mechanical spreading

Following the advection, diffusion and entrainment of oil particles, additional particle movement is needed to represent the mechanical spreading of oil above its terminal spreading thickness.

The volume of oil in each thickness map cell is calculated by summing the particles present in the cell, to form $V_{\text{oil}} := V_{\text{oil}}(x, y, t) : \delta\Omega \times \mathbb{R}_+ \rightarrow \mathbb{R}_+$, in units of barrels for the empirical equation. This is then used to calculate area in square meters in Lehr's modified fay-type spreading formula (Lehr et al., 1984), using the lower coefficient for a low wind case (as wind drift is accounted for elsewhere) and the average age of the oil in that cell $t_{\text{oil}} := t_{\text{oil}}(x, y, t) : \delta\Omega \times \mathbb{R}_+ \in \mathbb{R}_+$ in minutes from the spill start. The empirical slick area $A_{\text{oil}} := A_{\text{oil}}(x, y, t) : \delta\Omega \times \mathbb{R}_+ \rightarrow \mathbb{R}_+$ is found by computing

$$A_{\text{oil}} = 10^3 \left(2.27 \frac{\rho_{\text{water}} - \rho_{\text{oil}}}{\rho_{\text{oil}}} \frac{2}{3} V_{\text{oil}}^{\frac{2}{3}} t_{\text{oil}}^{-\frac{1}{2}} + 0.03 \frac{\rho_{\text{water}} - \rho_{\text{oil}}}{\rho_{\text{oil}}} \frac{1}{3} V_{\text{oil}}^{\frac{1}{3}} \left\| \vec{U}_{\text{wknots}} \right\|_2^{\frac{4}{3}} t_{\text{oil}} \right), \quad (27)$$

where \vec{U}_{wknots} is the wind velocity converted to knots and where the oil age in hours t_{oil} is capped to 48 hours, at which point mechanical spreading is minimal. Slick thickness in meters $\Gamma := \Gamma(x, y, t) : \delta\Omega \times \mathbb{R}_+ \rightarrow \mathbb{R}_+$ in the grid cell of area A_{oil} is then calculated as

$$\Gamma = \frac{V_{\text{oil}_{\text{m}^3}}}{A_{\text{oil}}}, \quad (28)$$

where $V_{\text{oil}_{\text{m}^3}}$ is the volume of oil in the cell converted to cubic meters. Depending on the oil type, if this thickness

exceeds that of the equilibrium, or terminal oil thickness then mechanical spreading is applied using Lardners Lagrangian method in the local cell (Lardner and Gunay, 2000):

$$\delta Q = 1.13 \left(\frac{\rho_{\text{water}} - \rho_{\text{oil}}}{\rho_{\text{water}}} \right)^{\frac{1}{3}} V_{\text{oil}_{\text{m}^3}}^{\frac{1}{3}} \frac{1}{4} t_{\text{oil}_{\text{sec}}}^{-\frac{3}{4}} \delta t, \quad (29a)$$

$$\delta R = \delta Q + 0.0034 \left\| U_{\text{wind}_{10}} \right\|_2^{\frac{4}{3}} \frac{3}{4} t_{\text{oil}_{\text{sec}}}^{-\frac{1}{4}} \delta t, \quad (29b)$$

$$x_{\text{new}} = x_0 + \delta Q \cos(\theta_{\text{wind}}) + \delta R \sin(\theta_{\text{wind}}), \quad (29c)$$

$$y_{\text{new}} = y_0 + \delta Q \sin(\theta_{\text{wind}}) + \delta R \cos(\theta_{\text{wind}}). \quad (29d)$$

For this empirical formula, t_{oil} is in seconds and $\theta_{\text{wind}} := \theta_{\text{wind}}(x, y, t) : \delta\Omega \times \mathbb{R}_+ \rightarrow \mathbb{R}$ is the wind angle, or bearing from north of \vec{U}_w . The distances $\delta Q \in \mathbb{R}$ and $\delta R \in \mathbb{R}$ represent the mechanical spreading and the augmented mechanical spreading from wind effects respectively. Equations within Sections 3.1, 3.2 and 3.3 have described the movement of oil particles in the surface and subsurface ocean, but have not accounted for any changing in oil properties through weathering or particle deposition on obstacles and shorelines.

3.4. Oil deposition

The model currently assumes zero particle movement once it enters a non-water cell. If the beach cell is considered saturated, the particle cannot enter (Chao, Shankar, and Wang, 2003) and remains afloat. This offers simple shore deposition, though particles cannot re-float once deposited.

3.5. Number of oil particles

The presence of random processes modelling oil turbulent diffusion and entrainment cause the spreading of oil particles to become a stochastic process in the simulation. Therefore the number of particles required in the simulation is not determined by the need for accurate reconstruction of a spill shape, but by the need to adequately sample the combined probability distribution function to resolve the process. The stochastic element is a combination of a 2D random walk, a 1D random walk and a dichotomous binomial distribution with a uniform distribution. These are horizontal turbulent diffusion, vertical turbulent diffusion and binary entrainment at a uniformly random depth.

First consider the horizontal turbulent diffusion random walk: Although the distance from origin is not accurately represented by a Normal distribution as samples cannot take values less than zero, the distribution of particles along an individual axis can be assumed Normal. The

horizontal diffusion Normal distribution has the parameters

$$\sigma_{\text{horz}} = (\sqrt{2} - 1)\sqrt{12D_h\delta t} \quad (30a)$$

and

$$\mu_{\text{horz}} = 0, \quad (30b)$$

forming the distribution $N(\mu_{\text{horz}}, \sigma_{\text{horz}}^2)$. Define the confidence interval $\alpha_{\text{horz}} \in \mathbb{R}$ and expected random walk movement $E_{\text{horz}} \in \mathbb{R}$ by

$$\alpha_{\text{horz}} = 0.05, \quad (31a)$$

and

$$E_{\text{horz}} = \frac{1}{2}\sqrt{12D_h\delta t}, \quad (31b)$$

then the number of samples needed to approximate the random walk process with a 95% confidence level is (NIST/SEMATECH, 2012):

$$n_{\text{horz}} \geq \left(\frac{1.96}{\alpha_{\text{horz}}E_{\text{horz}}}\right)^2 \sigma_{\text{horz}}^2. \quad (32)$$

Under typical simulation conditions in Beaufort scale 5 sea states, n_{horz} in (32) has a value of approximately 1000, which exceeds the samples needed to approximate the vertical turbulent diffusion, uniform entrainment depth and the number of samples required to apply the central limit theorem to the dichotomous binomial distribution of entrainment. Given the complex interaction between stochastic processes that would greatly increase the variance of the combined probability function, the negligible effect on computational time of increased numbers of oil particles and the implicit desire to improve the simulation accuracy and confidence limit, it is recommended that a minimum of 3000 particles be used. This also exceeds the sum of sample sizes needed for each random process in typical conditions.

3.6. The probability of oil presence

In a simulation realization identified by $S_n \in \mathbb{N}$, the presence of oil at a time-step $t_k \in \mathbb{R}_+$ in the cell at position $(x_i, y_j, z_w) \in \Omega$ is described by the binary random variable $O_p(x_i, y_j, z_w, t_k, S_n)$, which takes the value 0 when the oil volume in the cell at (x_i, y_j, z_w) is less than an arbitrary threshold value $\zeta_p \in \mathbb{R}_+$ (no oil present) and the value 1 when the oil volume in the cell is greater than ζ_p (oil is present), at time-step t_k . The binary random variable is described by

$$O_p(x_i, y_j, z_w, t_k, S_n) = \begin{cases} 0 & \text{when } \tilde{V}_{\text{oil}}(x_i, y_j, z_w, t_k, S_n) \leq \zeta_p, \\ 1 & \text{when } \tilde{V}_{\text{oil}}(x_i, y_j, z_w, t_k, S_n) > \zeta_p, \end{cases} \quad (33)$$

where the function $\tilde{V}_{\text{oil}}(x_i, y_j, z_w, t_k, S_n) : \Omega \times \mathbb{R}_+ \times \mathbb{N}_+ \rightarrow \mathbb{R}_+$ returns the volume of oil present in the discrete cell (x_i, y_j, z_w) at time t_k for realization S_n . Consequently, the evolution of oil presence across the spatial domain is

described by the stochastic process $\{O_p(\Omega, t_k, S_n)\}_{t_k \in \mathbb{R}_+}$, the set of binary random variables describing oil presence in the spatial domain Ω for each time-step t_k , for realization S_n . The presence of oil in a set of space and time $A \subseteq \Omega \times \mathbb{R}_+$ that may span multiple time steps, on a discrete mesh, is characterised by the binary random variable

$$\tilde{O}_p(A, S_n) = \begin{cases} 0 & \text{when } \sum_{x_i, y_j, z_w, t_k \in A} O_p(x_i, y_j, z_w, t_k, S_n) = 0, \\ 1 & \text{when } \sum_{x_i, y_j, z_w, t_k \in A} O_p(x_i, y_j, z_w, t_k, S_n) \neq 0. \end{cases} \quad (34)$$

Hence, $\tilde{O}_p(A, S_n)$ only takes value 0 if the volume oil in every cell is less than or equal to ζ_p for the entire spatio-temporal set A , or takes value 1 if the oil volume in any cell exceeds ζ_p at any time, in the realization S_n .

To inform sensor placement it is useful to describe the probability of oil presence in A , by utilising multiple realizations each of which is assumed to be an independent stochastic process. Multiple realizations are needed to examine model sensitivity to uncertain parameters, such as drift coefficients. The probability of oil volume exceeding ζ_p using $S_t \in \mathbb{N}$ realizations, $P(\hat{O}_p(A) = 1, S_t)$ is defined by

$$P(\hat{O}_p(A) = 1, S_t) = \frac{\sum_{S_n=1}^{S_n=S_t} \tilde{O}_p(A, S_n)}{S_t}. \quad (35)$$

To determine the number of realizations needed to adequately sample the random processes, the probability of oil presence sample variance after S_t realizations is calculated (Montgomery and Runger, 1994) by

$$\text{Var}(P(\hat{O}_p(A) = 1)) = \frac{1}{S_t - 1} \sum_{S_n=1}^{S_n=S_t} \left(P(\hat{O}_p(A) = 1, S_n) - \bar{P}(\hat{O}_p(A) = 1, S_n) \right)^2, \quad (36a)$$

with a maximum value across Ω of

$$\text{Var}_{\max}(P(\hat{O}_p(A) = 1)) = \max_{A \in \Omega} \left(\text{Var}(P(\hat{O}_p(A) = 1)) \right), \quad (36b)$$

where $\bar{P}(\hat{O}_p(A) = 1, S_t) = \frac{1}{S_t} \sum_{S_n=1}^{S_n=S_t} P(\hat{O}_p(A) = 1, S_n)$ is the mean probability of oil presence for S_t realizations. For the parameters of Table 2 and an oil threshold value of $\zeta_p = 0$, the maximum value of the variance (36b) with realization number decreases rapidly, then settles after $S_n \approx 200$ as in Figure 7. The variance distribution of (36a) displayed peaks at the trail and leading edges of the spill, as expected due to the changing in presence of oil across realizations compared to the overlap of spills at the spill centre. The variance in oil presence probability is used instead of the variance in oil presence, as a confidence

interval in oil probability describes a range of chance in oil presence and is more useful than a confidence interval in number of realizations with oil present.

3.7. The probability of oil particle drift location at a specific time

Another useful event to model is the surface location of a selected oil volume at a given time-step. Define the vector valued random variable $O_v(p_i, t_k, S_n) = [x_p, y_p] \in \delta\Omega$ to take the vector position of the oil particle index $p_i \in \mathbb{N}$ at the time-step t_k , with $x_p \in \mathbb{R}$ and $y_p \in \mathbb{R}$ the horizontal and vertical locations respectively, for a given realization S_n . The probability of an oil particle p_i to be within the discrete cell (x_i, y_j) at t_k , $P(O_v(p_i, t_k, S_n) \in (x_i, y_j))$, is defined by

$$P(O_v(p_i, t_k, S_n) \in (x_i, y_j)) = \frac{\sum_{p_i \in p_p(x_i, y_j, t_k, S_n)} V_{\text{particle}}(p_i, S_n)}{\sum_{p_i \in p_t(t_k, S_n)} V_{\text{particle}}(p_i, S_n)}, \quad (37)$$

where $p_p(x_i, y_j, t_k, S_n) : \delta\Omega \times \mathbb{R}_+ \rightarrow \mathbb{N}^{m_p}$ is a vector of particle indices present in the discrete spatio-temporal location and $p_t(t_k, S_n) \rightarrow \mathbb{N}^{m_t}$ is a vector of all particle indices at time t_k , with m_p and m_t being the number of oil particles present and the total number of oil particles respectively. The oil volume function $V_{\text{particle}}(p_i, S_n) : \mathbb{N}^{m_t} \rightarrow \mathbb{R}_+$ maps oil particle indices p_i to the oil volume they represent in the model. Evaluation of (37) for every cell in $\delta\Omega$ forms the probability mass function displayed in Figures 5 and 6. The probability of oil presence in cell (x_i, y_j) is obtained by averaging over the realizations of the stochastic process. The resulting probability is given by

$$P(\hat{O}_v(p_i, t_k) \in (x_i, y_j)) = \frac{1}{S_t} \sum_{S_n=1}^{S_n=S_t} P(O_v(p_i, t_k, S_n) \in (x_i, y_j)), \quad (38)$$

where $P(O_v(p_i, t_k, S_n) \in (x_i, y_j))$ is the evaluation of (37) for that realization index. This probability, $P(\hat{O}_v(p_i, t_k) \in (x_i, y_j))$, provides a further measure for route planning by indicating likely areas of high oil volume, while the probability of oil presence $P(O_p(x_i, y_j, z_w, t_k) = 1)$ defines likely areas of any oil exceeding a threshold ζ_p .

3.8. The mean location of the spill centre

A further vector valued random variable $O_m(t_k, S_n) = [x_m, y_m] \in \delta\Omega$ takes the value of the position of highest oil volume for realization S_n , where $x_m \in \mathbb{R}$ and $y_m \in \mathbb{R}$ are the horizontal and vertical locations of the highest volume position respectively. The value taken by $O_m(t_k, S_n)$ is one definition of the spill centre. Define the mean spill centre position across realizations by

$$\bar{O}_m(t_k) = \frac{1}{S_t} \sum_{S_n=1}^{S_n=S_t} O_m(t_k, S_n). \quad (39)$$

The mean spill centre position for 500 realizations is displayed in Figure 8.

4. Model simulation and results

The model is intended to guide sensing assets in the aftermath of maritime incidents and hence requires validation, with comparison against real-world data preferable (Spaulding, 2017). The Grande America oil spill of March 2019 provides a recent and observed incident to validate against. However due to the vessel's abandonment on the 11th March 2019 due to an onboard fire and the subsequent sinking in water depth of 4600m between 1500 and 1800 hours on the 12th March 2019, it is unclear exactly when the vessel sank, the oil leak occurred, or how much leaked. This information forms the initial conditions for the spill and can heavily affect simulation results.

For the model simulation it is assumed the fuel tanks became compromised as the hull split and sank and the worst case scenario is modelled: all 2200 tonnes of Heavy Fuel Oil carried by the Grande America is spilt in a short time-frame, from 1400 to 1600 hours on the 12th March 2019, at coordinates -5.7844° East, 46.0689° North. The model utilises Global Forecast System (GFS) wind velocities and Tide-Tech ocean velocities, with a North-West to South-East wave swell with significant wave height of 3m from National Centers for Environmental Prediction (NCEP) data. User specified parameters are presented in Table 2. The Grande America oil spill was observed by the Copernicus Sentinel 1 and 2 satellites on two occasions, on the 19th March 2019 the 5 day old slick is observed at approximately 45.439458° North, -4.283424° East and on the 23rd March 2019 the 11 day old slick is observed at 45.0826° North, -4.4559° East.

Due to the uncertainty surrounding the initial spill conditions and volume, emphasis is placed on the model accurately predicting the drift of a spill, with little importance placed on predicting the slick thickness or volume. The probability of oil drift location in a spatio-temporal domain is given by equation (37), this is evaluated for each grid-cell area at the indicated time to produce Figures 5 and 6. Figures 5 and 6 show accurate prediction of the slick locations, with high probability at 45.2000° North, -4.1850° East on the 19th March 2019, with the true location being 45.1857° North, -4.323424° East, $\approx 14\text{km}$ to the north west. For the 23rd March 2019, with no correction or reinitialisation from the true spill position on the 19th March, the model predicts a slick location at 45.0300° North, -4.2100° East, compared to the true position at 45.0826° North, -4.6559° East, 20km to the west of the predicted position. Errors of 15km and 20km for five and eleven day predictions, respectively, not unreasonable given the scale of the spill, the large size of the

domain, the lack of model correction or calibration and the model's intended purpose for predictions over much shorter time-scales (hours to a day). The 288 hour prediction took 568 seconds to compute in MATLAB, on a Windows 10, i7-6700k CPU desktop computer, this includes computation time for the wind, wave and ocean hydrodynamic models across 2688 surface nodes, extrapolated to 534912 sub-surface nodes. All parameters were within ranges acceptable to literature and use their values within Table 2.

To investigate the sensitivity to the spill parameters and the diffusion, wind and ocean current coefficients of equation (13), 500 simulation realizations using simultaneous sampling of the random variable coefficients of Table 2 were utilised to get a probability of oil presence map (35) across the set of random variables. Figure 8 shows that the model is accurate for the Grande America spill within the typical bounds for drift parameters and that the default coefficient values slightly overestimate oil movement up to the 19th March 2019 when comparing the results of Figures 5 and 8.

As demonstrated by the Grande America spill, data is scarce on spill components, environmental data, contaminant position and thickness following a real incident, with even international scale incidents only becoming well observed and documented several days after the incident.

Given that the model may be required to make predictions for spills in remote areas, where existing hydrodynamic models may be inaccurate or non existent, the model is now compared to the industry standard model GNOME as a benchmark to see if it provides similar predictions when provided with the same inputs. As a further comparison and as a pointer to future work, a test is performed to see if the model can offer similar results when given erroneous inputs (hydrodynamic data without tide flow in a river delta for example), by using real-time sensory feedback from sensors taking data from a twin GNOME simulation with accurate input data.

This section also presents comparison of several spill simulations using this oil model and GNOME, utilising three sets of data, Global Forecast System (GFS) wind velocities, HYCOM ocean velocities (that contain no tidal flow data, only circulation flow) and Tide-Tech ocean velocities. As large data set acquisition is unlikely to be available in deployment due to data transmission constraints, both the HYCOM and Tide-Tech ocean data results are assumed to be available as surface velocity only. Both sets include Ekman currents and therefore Ekman currents are omitted from the surface dynamics, but a spiral is calculated sub-surface to model oil slick shear separation between surface and sub-surface particles. Both models utilise the same number of particles, representing the same volume of oil each and released at the same leak rate from the same location. Therefore, particle positions can be utilised for comparative purposes.

Experiment 1 is a 3-day simulation of a 100 barrel spill released 1 mile south of Lamma Island, Hong Kong, at

0330 hours on the 8th January 2019 carried out as a contingency for the Aulac Fortune oil tanker explosion. The oil models are both forced by HYCOM ocean current data and GFS wind data and their similarity displayed in Figure 9 validates the resolving of external data in the environment model (Section 2) and oil model (Section 3).

Experiment 2 demonstrates the sensitivity of oil models to the environment model they are driven by. The GNOME model has been driven by the GFS wind data and by Tide-Tech ocean current data sets that include a harmonic tide component reflecting the important effect of the Zhujiang river estuary. The raw Tide-Tech data has been modified to a higher resolution and resolved around islands using the Navier-Stokes simulation of Section 2, with original values preserved where possible. Note the large discrepancies between the GNOME results of Figure 10 and Figure 9, with the majority of flow passing to the north of the island cluster at 22N 113.7E when tidal flow is present.

Experiment 3 demonstrates the effectiveness of sensors when informing the model described here-in, to deliver accurate results even when prior information is inaccurate. The model is forced by HYCOM ocean current data (that lack strong tidal components) and GFS wind data, but well-guided mobile sensors capable of measuring wave, wind and current properties and oil thickness are capable of minimising the error in oil estimation that results from external data differences. The methodology utilises SCEM and is detailed in future work. The four sensors measure flow and oil values at point locations from the GNOME Experiment 2 run, at regular intervals of every 15 minutes, and are constrained by their maximum speed of 50mph. It is assumed the sensors are capable of measuring the flow properties perfectly and their measurements inform a time-varying Kalman Filter utilising a modal decomposition model of SCEM, to estimate SCEM states. Figure 11 displays the similarity between the spill particles of the model and those of the GNOME simulation, with both the spills leading edge and dominant concentrations matching, including having a majority flow around the north of the island cluster at 22N 113.7E, despite tidal flow being absent from input data in this model.

5. Conclusion

Motivated by the need to monitor environment properties or pollutants in the aftermath of maritime incidents, a model-based adaptive monitoring strategy is developed for the the emerging application of mobile sensors. This paper presents the Sheffield Combined Environment Model (SCEM), the environment and oil model component of the monitoring methodology used in Figure 11, for the purpose of providing online control guidance to assets with minimal supporting data. The new model is described, giving equations and algorithm in both flow chart (Figure 1) and pseudocode (Algorithm 1). The model is then demonstrated to accurately predict a real-world oil spill in

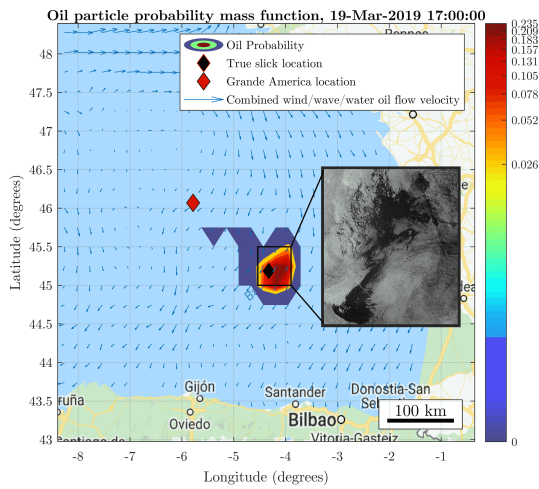


Figure 5: The probability mass function of oil particle drift (37) from the SCEM simulation for 17:00 on 19th March 2019, 5 days after the spill released, using a log scale and with the real position marked. Note the similarity in location to the real slick location on the 19th March. Map data ©2019 Google, Inst. Geogr. Nacional. Contains modified Copernicus Sentinel data (2019), processed by ESA, CC BY-SA 3.0 IGO.

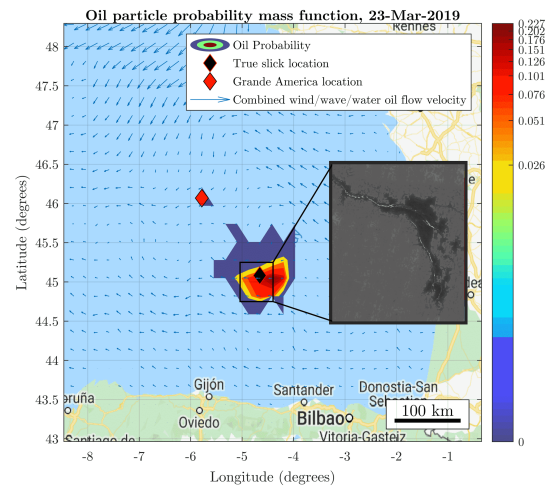


Figure 6: The probability mass function of oil particle drift (37) from the SCEM simulation for the 23rd March 2019, 11 days after the spill released, using a log scale and with the real position marked. Note the similarity in location to the real slick location on the 23rd March. Map data ©2019 Google, Inst. Geogr. Nacional. Contains modified Copernicus Sentinel data (2019), processed by ESA, CC BY-SA 3.0 IGO.

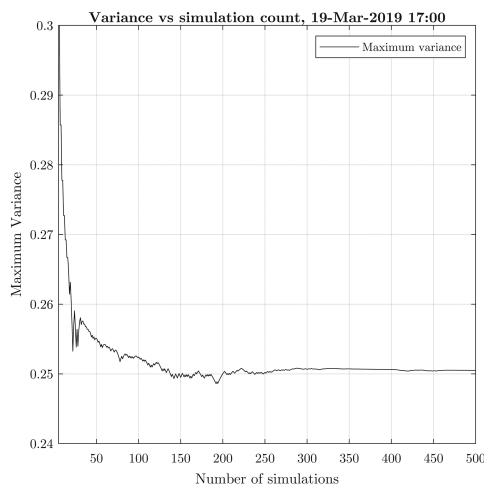


Figure 7: The plot showing the decay of the maximum variance of oil presence (36b) across 500 SCEM simulations for 17:00 on the 19th March 2019, 5 days after the spill released. Note the rapid decay and convergence, settling around 200 simulations.

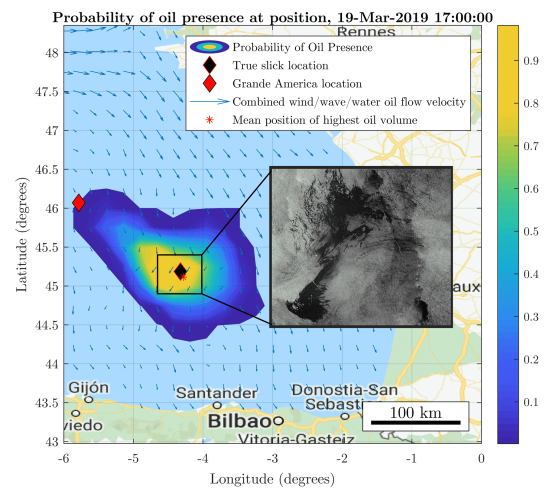


Figure 8: The combined probability map of oil presence (35) for 17:00 on the 19th March 2019, 5 days after the spill released, with the real position marked. Each SCEM simulation was a sampling of spill parameters in Table 2. Note the similarity in location of the highest probability and mean spill position to the real slick location on the 19th March. Map data ©2019 Google, Inst. Geogr. Nacional. Contains modified Copernicus Sentinel data (2019), processed by ESA, CC BY-SA 3.0 IGO.

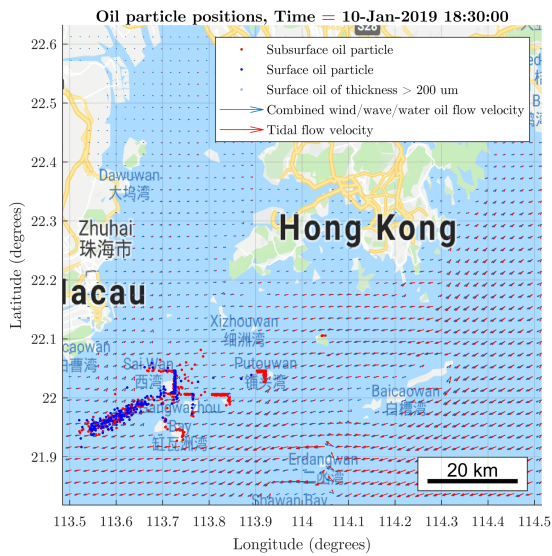


Figure 9: The model and GNOME simulation results for a 3-day simulation of a 100 barrel spill released 1 mile south of Lamma Island, Hong Kong, at 0330 hours on the 8th January 2019. Both models has been forced by GFS wind velocities and HYCOM ocean velocities. Note the presence of oil on all the same islands and positions of the leading edge of the spill. Map data ©2019 Google.

the Bay of Biscay 2019 and give similar results to an industry standard oil model GNOME when given the same input data for a spill near Hong Kong 2019.

Furthermore, a sensing strategy developed using SCEM is shown to be capable of delivering an accurate estimation of oil positions when given inaccurate external forcing data. This provokes further research into optimal sensor placement and sensor feedback methods through application of optimisation, estimation and data fusion fields of work.

References

- Baldauf, M and G Zängl (2012). “Horizontal nonlinear Smagorinsky diffusion”. In: *COSMO newsletter* 2.April, pp. 3–7.
- CERC (2017). *URBAN CANOPY FLOW SPECIFICATION*. Tech. rep. August, pp. 1–7.
- Chao, Xiaobo, N. Jothi Shankar, and Sam S. Y. Wang (2003). “Development and Application of Oil Spill Model for Singapore Coastal Waters”. In: *Journal of Hydraulic Engineering* 129.7, pp. 495–503.
- Courant, R, K O Friedrichs, and H Lewy (1967). “On the partial difference equation of mathematical physics”. In: *IBM Journal of Research and Development* 11.215-234, pp. 32–74. arXiv: AD0832715.

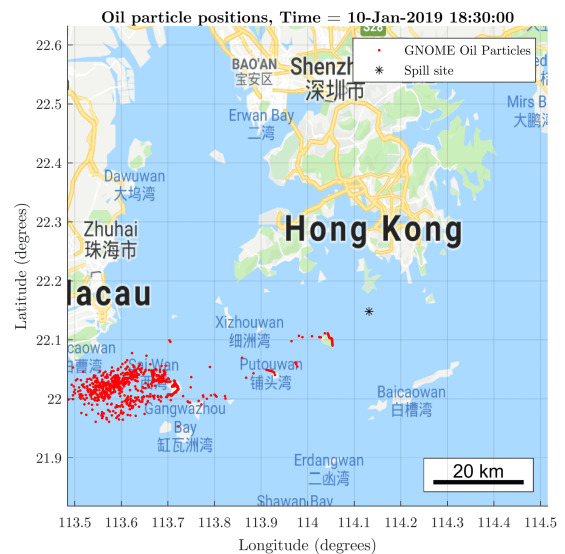


Figure 10: GNOME results for a 3-day simulation of a 100 barrel spill released 1 mile south of Lamma Island, Hong Kong, at 0330 hours on the 8th January 2019. GNOME has been forced by GFS wind velocities and Tide-Tech ocean velocities that include tidal flow. Map data ©2019 Google.

- De Dominicis, M. et al. (2013a). “MEDSLIK-II, a Lagrangian marine surface oil spill model for short-term forecasting-Part 1: Theory”. In: *Geoscientific Model Development* 6.6, pp. 1851–1869.
- De Dominicis, M. et al. (2013b). “MEDSLIK-II, a Lagrangian marine surface oil spill model for short-term forecasting-Part 2: Numerical simulations and validations”. In: *Geoscientific Model Development* 6.6, pp. 1871–1888.
- Delvigne, G. A L and C. E. Sweeney (1988). “Natural dispersion of oil”. In: *Oil and Chemical Pollution* 4.4, pp. 281–310.
- Elliott, Alan J. (1986). “Shear diffusion and the spread of oil in the surface layers of the North Sea”. In: *Deutsche Hydrographische Zeitschrift* 39.3, pp. 113–137.
- EMSA (2018). *Annual Overview of Marine Casualties and Incidents 2018*. Tech. rep. European Maritime Safety Agency, pp. 1–135.
- F. Harlow and J. Welch (1965). “Numerical Calculation of Time-Dependent Viscous Incompressible Flow of Fluid With Free Surface”. In: *Physics of Fluids* 8.1, pp. 2182–2189.
- Fingas, Merv and Carl Brown (2014). “Review of oil spill remote sensing”. In: *Marine Pollution Bulletin* 83.1, pp. 9–23.
- French McCay, D. et al. (2016). “Modeling Oil Fate and Subsurface Exposure Concentrations from the Deepwater Horizon Oil Spill”. In: *AMOP Technical Seminar*.

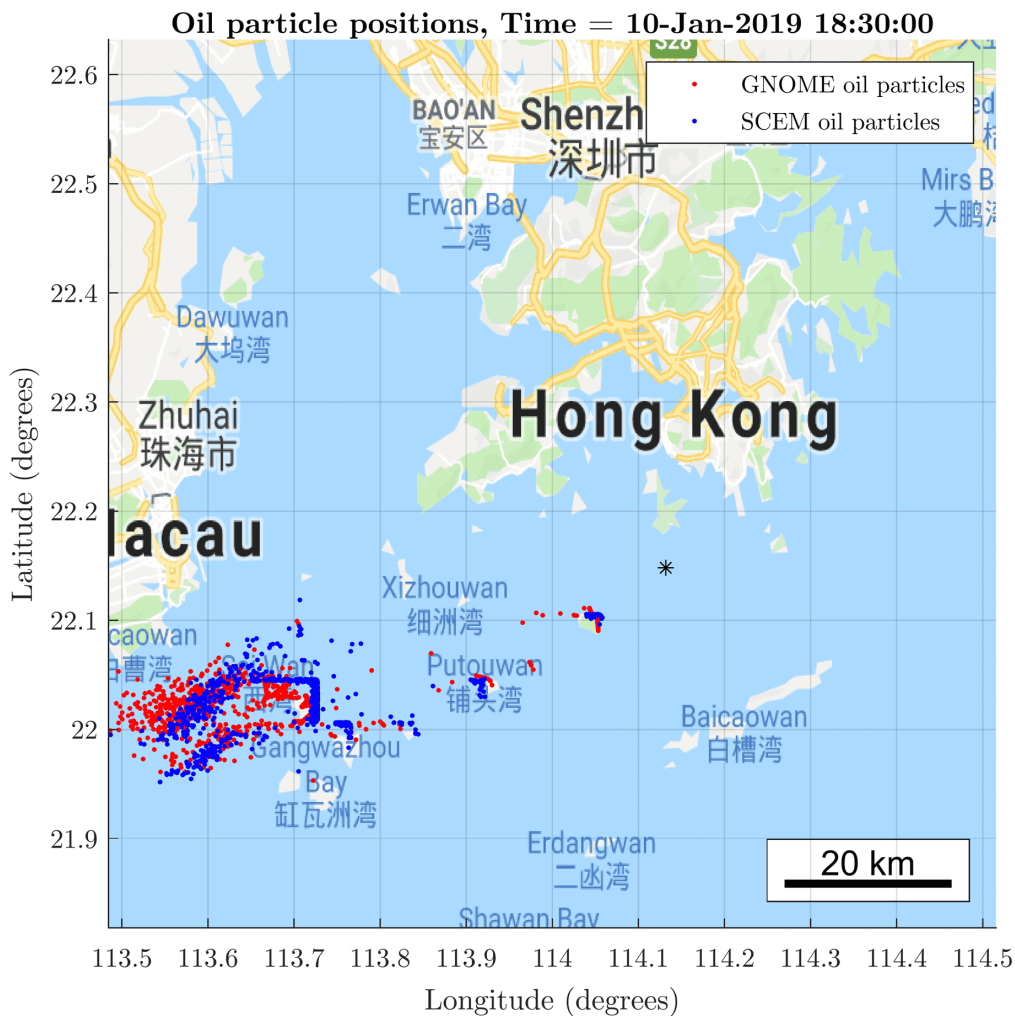


Figure 11: The model and GNOME simulation results for a 3-day simulation of a 100 barrel spill released 1 mile south of Lamma Island, Hong Kong, at 0330 hours on the 8th January 2019. The model has been forced by GFS wind velocities and HYCOM ocean velocities, while GNOME has been forced by GFS wind velocities but Tide-Tech ocean velocities that include tidal flow. Note the presence of oil on all the same islands, concentration and positions of the leading edge of the spill. Map data ©2019 Google.

- Heins, Peter H and Bryn Ll Jones (2016). “SWEM : A Multiphysics Sea-Surface Simulation Environment”. In: *UKACC 11th International Conference on Control*.
- Hunter, J. R., P. D. Craig, and H. E. Phillips (1993). “On the use of random walk models with spatially variable diffusivity”. In: *Journal of Computational Physics* 106.2, pp. 366–376.
- ITOPF (2011). *Aerial Observation of Marine Oil Spills*. Tech. rep. 1. ITOPF, p. 12.
- (2014). *Aerial Surveillance - ITOPF*.
- (2019). *Oil Tanker Spill Statistics 2018*. Tech. rep. January. ITOPF, p. 12.
- Kim, Tae Ho et al. (2014). “Analysis of the contribution of wind drift factor to oil slick movement under strong tidal condition: Hebei Spirit oil spill case”. In: *PLoS ONE* 9.1, pp. 1–14.
- Kirincich, Anthony R. and John A. Barth (2008). “Time-Varying Across-Shelf Ekman Transport and Vertical Eddy Viscosity on the Inner Shelf”. In: *Journal of Physical Oceanography* 39.3, pp. 602–620.
- Lamb, Horace (1895). “Hydrodynamics”. In: *Journal of Chemical Information and Modeling* 53.9, pp. 468–470. arXiv: arXiv:1011.1669v3.
- Lardner, R W and N Gunay (2000). “Gulfspill Version 2.0 : a software package for oil spills in the Arabian Gulf”. In: *Environment Modelling & Software* 15, pp. 425–442.
- Laruelle, Franck (2011). “Responding to Spills in Remote Locations: GULSER ANA (Madagascar) & OLIVA (South Atlantic)”. In: *ITOPF Library*, pp. 1–12.
- Lehr, W. et al. (2002). “Revisions of the ADIOS oil spill model”. In: *Environmental Modelling & Software* 17.2, pp. 189–197.
- Lehr, W. J. et al. (1984). “A new technique to estimate initial spill size using a modified fay-type spreading formula”. In: *Marine Pollution Bulletin* 15.9, pp. 326–329.
- Li, Yan, Jiang Zhu, and Hui Wang (2013). “The impact of different vertical diffusion schemes in a three-dimensional oil spill model in the Bohai Sea”. In: *Advances in Atmospheric Sciences* 30.6, pp. 1569–1586.
- Lonin, Serguei A. (1999). “Lagrangian model for oil spill diffusion at Sea”. In: *Spill Science and Technology Bulletin* 5.5-6, pp. 331–336.
- Madec, Gurvan (2011). *NEMO Ocean Engine: version 3.3*. Tech. rep. l’Institut Pierre-Simon Laplace.
- Marsooli, Reza (2017). “Some questions on ”A Coupled Circulation-Wave Model for Numerical Simulation of Storm Tides and Waves (2017)””. In: [email].
- Marsooli, Reza et al. (2017). “A Coupled Circulation-Wave Model for Numerical Simulation of Storm Tides and Waves”. In: *Journal of Atmospheric and Oceanic Technology*.
- Mellor, George (2003). “The Three-Dimensional Current and Surface Wave Equations”. In: *Journal of Physical Oceanography* 33.9, pp. 1978–1989.
- Mellor, George L., Mark a. Donelan, and Lie-Yauw Oey (2008). “A Surface Wave Model for Coupling with Numerical Ocean Circulation Models”. In: *Journal of Atmospheric and Oceanic Technology* 25.10, pp. 1785–1807.
- Mellor, George L. and Yamada Tetsuji (1982). “Development of a Turbulence Closure Model for Geophysical Fluid Problems”. In: *Reviews of Geophysics and Space Physics* 20.4, pp. 851–875.
- Montgomery, D. C. and G. C. Runger (1994). *Applied statistics and probability for engineers*. John Wiley, p. 201.
- Moore, Andrew M. et al. (2011). “The Regional Ocean Modeling System (ROMS) 4-dimensional variational data assimilation systems”. In: *Progress in Oceanography* 91.1, pp. 34–49.
- NIST/SEMATECH (2012). *NIST/SEMATECH e-Handbook of Statistical Methods*.
- Pond, Stephen and George L Pickard (2013). *Introductory dynamical oceanography*. Elsevier.
- Proctor, Roger, Roger A. Flather, and Alan J. Elliott (1994). “Modelling tides and surface drift in the Arabian Gulf-application to the Gulf oil spill”. In: *Continental Shelf Research* 14.5, pp. 531–545.
- Rasmussen, Dorte (1985). “Oil Spill Modeling—a Tool for Cleanup Operations”. In: *International Oil Spill Conference Proceedings* 1985.1, pp. 243–249.
- Reed, Mark et al. (2000). “OSCAR2000: a multi-component 3-dimensional Oil Spill Contingency and Response model”. In: *Arctic and Marine Oilspill Program Technical Seminar*.
- Smith, Stuart D. (1988). “Coefficients for sea surface wind stress, heat flux, and wind profiles as a function of wind speed and temperature”. In: *Journal of Geophysical Research: Oceans* 93.C12, pp. 15467–15472.
- Spaulding, Malcolm L. (2017). “State of the art review and future directions in oil spill modeling”. In: *Marine Pollution Bulletin* 115.1-2, pp. 7–19.
- Stam, Jos (2001). “A Simple Fluid Solver Based on the FFT”. In: *Journal of Graphics Tools* 6, pp. 43–52.
- Taylor, Publisher et al. (2003). “A multiphase oil spill model Un modèle multiphase de nappe d ’ huile”. In: *Journal Of Hydraulic Research* 41.2, pp. 115–125.
- Thiébaud, Maxime and Alexei Sentchev (2016). “Tidal stream resource assessment in the Dover Strait (eastern English Channel)”. In: *International Journal of Marine Energy* 16. February 2018, pp. 262–278.
- Tkalich, Pavlo and Eng Soon Chan (2002). “Vertical mixing of oil droplets by breaking waves”. In: *Marine Pollution Bulletin* 44.11, pp. 1219–1229.
- Topouzelis, Konstantinos and Suman Singha (2016). “Oil spill detection : past and future trends”. In: *ESA Living Planet Symposium* SP-740.
- Wang, Jinhua and Yongming Shen (2010). “Modeling oil spills transportation in seas based on unstructured grid, finite-volume, wave-ocean model”. In: *Ocean Modelling* 35.4, pp. 332–344.
- Weatherly, Georges L. (1975). *A Numerical Study of Time-Dependent Turbulent Ekman Layers over Horizontal and Sloping Bottoms*.

- Webb, A. and B. Fox-Kemper (2011). “Wave spectral moments and Stokes drift estimation”. In: *Ocean Modelling* 40.3-4, pp. 273–288.
- Wu, Jin (1975). “Wind-induced drift currents”. In: *Journal of Fluid Mechanics* 68.01, pp. 49–70.
- (1980). *Wind-Stress coefficients over Sea surface near Neutral Conditions—A Revisit*.
- Zhang, Yanmin et al. (2015). “The damping model for sea waves covered by oil films of a finite thickness”. In: *Acta Oceanologica Sinica* 34.9, pp. 71–77.

```

Result: Forwards ocean and contaminant simulation with external/sensor data
/* INITIALISE */
read user parameters (domain bounds, empirical parameters, see Table 2);
load external data files (domain bathymetry, external flow forcing data);
initialise domain;
foreach domain grid cell do
    | initialise SWEM wave model;
    | set start date state values;
end
load time-varying contaminant source file (oil type, source location, leak rate);
/* RUN SIMULATION */
while start time ≤ current time ≤ end time do
    /* CURRENT STATES */
    get predicted state values for current time;
    get external and/or sensor state values for current time;
    correct state values using external and/or sensor values at current time;
    calculate ekman wind value for each grid cell at current time (7);
    save state values for current time;

    /* CURRENT OIL SPILL */
    get oil particles for current time;
    get external and/or sensor oil values for current time;
    correct oil spill particles using external and/or sensor values at current time;
    save oil particles for current time;

    /* PREDICT NEXT OIL SPILL */
    get corrected state values for current time;
    calculate time-step;
    calculate velocity profiles at oil containing grid cells at current time (3), (6), (22);
    simulate SWEM at oil containing grid cells at current time;
    calculate oil diffusion coefficient at oil containing grid cells at current time (17a)(17d);
    calculate total oil velocity profile at oil containing grid cells at current time (13);
    calculate diffusion correction velocity at oil containing grid cells at current time (14);
    add source oil particles for time-step;
    foreach oil particle do
        | if oil particle is entrained into water column (25) then
            | insert oil particle at calculated depth, set buoyancy to 0 for time-step;
        | end
        | advect oil particle by current time local (total oil velocity + diffusion velocities + correction velocity +
            | buoyancy velocity) for time-step (13);
    end
    calculate oil spill thickness and volume for each grid cell (27);
    foreach oil particle do
        | advect oil particle by local mechanical spreading (29);
    end
    calculate oil spill thickness and volume for each grid cell (27);
    increase oil particles age;
    save estimate oil particles for next time;

    /* PREDICT NEXT STATES */
    simulate ocean and wind flow for time-step (1a);
    save predicted state values for next time;

    /* STEP TIME */
    step forward current time by time-step;
end

```

Algorithm 1: Pseudocode of the fluid model, simulating forwards in time.

America Grande simulation parameters			Units
Symbol	Description	Value	Nominal distribution within bounds
α_{w_0}	Oil wind advection coefficient	0.02	$\alpha_{w_0} \sim \bar{U}(0.005, 0.03)$
α_{c_0}	Oil current advection coefficient	1.0	$\alpha_{c_0} \sim U(0.9, 1.1)$
c_{smag}	Diffusion empirical parameter	0.1	$c_{\text{smag}} \sim U(0.01, 0.3)$
t_0	Spill leak start date	March 12th 2019 - 03:30:00	$t_0 \sim U(11/03/19 - 22:00:00, 12/03/19 - 17:00:00)$
t_f	Spill leak end date	March 12th 2019 - 16:30:00	$t_f \sim U(12/03/19 - 12:00:00, 12/03/19 - 18:00:00)$
V_T	Total spill volume	2200	$V_T \sim U(10, 2200)$
n_x, n_y, n_z	Domain nodes	$64 \times 42 \times 200$	-
Ω	Domain size	664.3×443.0	-
-	Oil Properties	Heavy Fuel Oil (No. 6 Fuel oil)	km
-	-	-	-

Table 2: Tabulation of parameters used in the Grande America oil spill simulation.